ACCSCIENCE PUBLISHING

Materials Science in Additive Manufacturing

ORIGINAL RESEARCH ARTICLE

Effects of heat treatment on microstructure and mechanical properties of 17-4PH/IN625 bimetallic parts fabricated through extrusion-based sintering-assisted additive manufacturing

Yulin Liu, Dayue Jiang, and Fuda Ning*

Department of Systems Science and Industrial Engineering, State University of New York at Binghamton, Binghamton, New York, United States of America

Abstract

The mechanical properties of bimetallic composites are significantly influenced by their interfacial morphologies. This study delves into the impact of various heat treatment conditions on the microstructure and mechanical attributes of steel/nickel bimetallic (17-4PH/IN625) components produced through extrusion-based sintering-assisted additive manufacturing (ES-AM). The bimetallic composites were annealed at 1150°C for 1, 4, and 8 h, followed by an aging treatment at 482°C for samples annealed for 8 h. After annealing, microstructural heterogeneities, including variations in grain size and elemental distribution within the transition zone close to the interface, were observed. It was found that in the diffusion transition zone between the two alloy layers, the diffusion of iron (Fe) and nickel (Ni) elements increased with longer holding times, as corroborated by microhardness tests and quantified through theoretical parabolic diffusion law. The transition zone exhibited two distinct areas: an Fe-predominant zone and a Ni-predominant zone, with the latter containing oxides and molybdenum (Mo)- and niobium (Nb)-rich precipitates. No new phases emerged post-heat treatment; however, shifts in peak due to stress relaxation and the emergence of precipitates were identified through X-ray diffraction (XRD) observations. Microhardness within the transition zone increased following heat treatment, peaking at 186 $HV_{1.0}$ after a 4-h annealing. The optimal heat treatment condition was identified as 1150°C for 4 h, which facilitated the development of uniform microstructures and improved bonding strength. This study demonstrates an enhanced interfacial bonding strength in 17-4PH and IN625 bimetallic parts manufactured through ES-AM, suggesting their wide-ranging potential applications in industry.

Keywords: Bimetallic composites; Extrusion-based sintering-assisted additive manufacturing; ES-AM; Heat treatment; Interface bonding; Diffusion zone

***Corresponding author:**
Fuda Ning
(fning@binghamton.edu)

Citation: Liu Y, Jiang D, Ning F. Effects of heat treatment on microstructure and mechanical properties of 17-4PH/IN625 bimetallic parts fabricated through extrusion-based sintering-assisted additive manufacturing. *Mater Sci Add Manuf.* 2024;3(2):3281. doi: 10.36922/msam.3281

Received: March 27, 2024

Accepted: April 29, 2024

1. Introduction

The demand for hybrid structures containing a combination of varied metal materials has increased to address the requirements of multiple industrial applications.[1] Bimetallic structures offer several advantages, such as superior structural robustness, improved mechanical strength, and improved economic efficiency compared to components manufactured from a single metal alloy.[2] Additive manufacturing (AM) techniques, categorized into fusion-state and solid-state AM methods, have been utilized to produce bimetallic parts. Fusion-based processes such as directed energy deposition (DED) and powder bed fusion (PBF) utilize high-energy sources such as electrons, wire arcs, and lasers to rapidly melt feedstocks, which then solidify on the substrate to form the desired part.[3] However, due to the varying thermal coefficients of bimetallic parts, the intense energy input and rapid melting and solidification processes often result in cracks and brittle failures.[4] Hybrid cold spray AM is a solid-state AM technique where micron-sized particles are accelerated to high velocities by high-pressure, low-temperature gas, impacting a substrate and undergoing plastic deformation to form a coating layer by layer.[5] Extrusion-based sintering-assisted additive manufacturing (ES-AM) employs a printing-debinding-sintering process, utilizing sintering temperatures lower than the melting point to handle bimetallic parts.[6] This approach allows for sufficient element diffusion during the sintering process, typically resulting in smoother interface surfaces and fewer intermetallic phases.[7] In addition, ES-AM offers benefits such as ease of operation, reduced risk, and an environmentally friendly manufacturing process.[8-10]

Several researchers have investigated the fabrication of bimetallic parts with fewer defects and cracks in the interface using ES-AM. Bimetallic components comprising low- and high-carbon steel have been synthesized through ES-AM; yet, the quality of the resultant part was compromised due to suboptimal optimization of process parameters, particularly in the co-sintering process.[11] Employing a copper infiltration technique, a composite structure featuring a high carbon steel exterior and a copper channel was engineered to fulfill the requirements of an injection mold, necessitating adequate mechanical strength, stiffness, and wear resistance, coupled with superior thermal conductivity.[12] In prior investigations, 17-4PH and IN625 were processed through ES-AM to fabricate a bimetallic component with a smooth interface and cohesive bonding devoid of conspicuous cracks.[7] 17-4PH stainless steel (SS) boasts high strength, hardness, and relatively good corrosion resistance, although it may have reduced elongation and temperature stability.[13] Meanwhile, IN625, a nickel-based superalloy, excels in corrosion resistance and high-temperature performance with reduced strength, commonly employed in aerospace and industrial sectors.[14] By combining these two materials in a bimetallic structure, the aim is to enhance mechanical properties, corrosion resistance, and temperature stability, catering to a broad spectrum of applications ranging from engine components to structural parts in harsh environments.[15] In addition, the thermal expansion coefficients of IN625 and 17-4PH are relatively close, with IN625 nickel-based superalloy at approximately 12.8×10^{-6}/°C[16] and 17-4PH SS at about $10.8 - 11.0 \times 10^{-6}$/°C.[17] This similarity in thermal expansion coefficients means that these two materials tend to expand and contract at similar rates in response to temperature changes, thereby reducing interface stress and minimizing the likelihood of cracks and defects. The co-sintering process in ES-AM is utilized to establish interface bonding, concurrently minimizing thermal stress and the development of intermetallic phases, due to its operation at relatively low temperatures. These lower temperatures can impede atomic diffusion, leading to pore formation and reduced interface bonding strength. The interface thus emerges as a critical factor in determining the structural integrity of dissimilar metal materials, acting as an essential conduit for the transfer of electricity, heat, damping, and other properties.[9,18-20]

Numerous studies have investigated the microstructure of interfaces and the mechanical properties of bimetallic parts made from SS and Inconel alloy, which were fabricated using various AM techniques. In a bimetallic part fabricated through hybrid DED and thermal milling, consisting of IN718 and 316L, diffusion layers were observed with a significant width of 450 mm, featuring a microstructural transition from columnar to equiaxed dendrites. Niobium (Nb) and molybdenum (Mo) precipitates were identified in the Inconel near the interface, with no other phases detected.[21] In the interface of a 304SS/IN738L bimetal fabricated by DED, an architecture featuring soft and stiff lamellae with inherent interfacial defects was observed, resulting from partial solute mixing and intricate fluid dynamics in the melt pool during rapid solidification.[22] In bimetallic materials composed of 316L and IN625, printed using DED, two types of interfaces were identified: one showing a gradual compositional change with IN625 grains growing epitaxially on 316L grains, and the other exhibiting a sudden compositional shift that encourages bidirectional nucleation and grain growth, leading to a high susceptibility to cracking.[23] In a bimetallic SS/nickel (Ni) alloy manufactured through PBF, no intermediate softening from ferrite phase formation occurred, but a decrease in hardness at the 316L side was noted, resulting from the thermal effects of manufacturing nickel alloy. In addition, MC carbides form in Ni-based superalloys during slow solidification due to the strong affinity of carbon for these metallic elements.[24] Bimetallic parts made of IN718 and high-carbon steel have been produced using ES-AM, which revealed a layered microstructure in partially sintered high-carbon steel and IN718 particles due to the diffusion of Ni and chromium (Cr) toward the steel granules.[25]

Heat treatment techniques are utilized to enhance bimetallic bonding by increasing the thickness of the diffusion zone and refining the intermetallic phase composition. The bimetallic assembly comprising SS316L and IN625, fabricated through arc welding, was heated to 970°C to facilitate the transformation of δ-ferrite into the austenite phase in SS316L, thereby improving the bond strength over the as-fabricated sample.[26] The process of normalizing applied to the IN625/carbon steel bimetallic joint resulted in the recrystallization of the constituent materials, along with the emergence of a diffusion zone and the precipitation within IN625.[27] After heat treatment, the bimetallic parts made of Ni-based superalloy and SS exhibited a secondary phase (Nb-rich phase) near the fusion boundary in the heat-affected zone on the Inconel side with higher hardness values.[28] Heat treatment effectively diminishes residual stresses and improves the toughness of aluminum (Al) bronze-steel bimetallic structures produced through AM, resulting in a sample with reoriented grains and a more uniform microstructure.[29] Varying the temperature or duration of heat treatment led to different levels of bonding strength at the interface. A continuous layer of titanium aluminide ($TiAl_3$) intermetallic was formed in the interface of Al/Ti bimetallic during specific heat treatment conditions, and the shear strength was governed by the strength of Al, with minimal impact from changes in the interlayer thickness.[30] The bonding behavior of a copper (Cu)/Al/Cu clad composite was investigated under different heat treatment temperatures, uncovering significant formation of intermetallic layers following specific heat treatment cycles, such as annealing at 500°C, leading to higher ductility and relatively high strength.[31] For a bimetallic part consisting of SS and carbon steel, the diffusion transition zone exhibited a rising trend with increasing annealing temperature, resulting in enhanced interfacial shear strength and improved ductility; however, it had a less pronounced effect on impeding fatigue crack propagation along the interface.[32] Heat treatment between 800°C and 1100°C for 30 min to 2 h significantly improved the properties of a bimetallic low-carbon steel and austenitic-SS structure, increasing its ultimate tensile strength by 35% and elongation by 250%.[33]

Nevertheless, there is insufficient research on the effects of heat treatment on the microstructure and mechanical properties of 17-4PH/IN625 bimetals produced through ES-AM. The co-sintering process, conducted at relatively low temperatures, results in pore formation and weaker bonding strength, necessitating heat treatment to enhance bonding strength and overall material properties. Consequently, this study aimed to investigate 17-4PH/IN625 bimetallic composites fabricated via ES-AM. It presents a comparative analysis elucidating the effects of heat treatment on the interfacial characteristics of bimetallic composites, with a focus on elemental diffusion, transition zone thickness, and microhardness evolution. To facilitate the expansion of the diffusion zone, specific heat treatment conditions were explored, including a homogenization treatment at 1150°C, with varying dwell times and cooling rates, followed by an aging treatment to establish an optimized heat treatment procedure for superior interfacial bonding strength.

2. Materials and methods

2.1. Materials and fabrication procedures

In this study, 17-4PH SS and IN625 filaments were procured from Markforged Corporation., (USA) consisting of metal powders combined with a consistent binder system comprised of wax and polyethylene. These filaments were fabricated using a dual-nozzle desktop 3D printer (F350, Creatbot, China) with a heated nozzle capable of reaching temperatures up to 450°C. An illustrative diagram of the manufacturing process is presented in Figure 1A. The 17-4PH SS filament was on the left and first extruded through a heated nozzle to reach a thickness of 2 mm with a layer thickness of 0.1 mm. Then, IN625 was printed using the right nozzle to deposit onto 17-4PH parts with a thickness of 0.1 mm. Finally, the overall size of parts is 15 × 15 × 4 mm^3, as shown in Figure 1D. The material properties for each filament and specific printing settings employed for each material are documented in Table 1. The processes of binder removal and solid-state sintering were carried out utilizing the Markforged production equipment (Metal X™ System, USA). A tailored sintering profile for IN625 alloy was applied due to its lower melting point compared to 17-4PH, with the entire procedure lasting 29 h. To achieve a denser structure during sintering, a smaller component with a thickness of 2 mm was placed on top of the bimetallic part. The printed and sintered bimetallic parts are presented in Figure 1B and C. The alloy compositions for 17-4PH and IN625 feedstocks are listed in Table 2. In addition, the properties of single metals are listed in Table 3 for comparison with bimetallic parts.

The heat treatments were conducted at a steady temperature of 1150°C and a heating rate of 10°C/min, with durations of 1, 4, and 8 h, labeled as HT1, HT4, and HT8, respectively. The utilization of this high constant temperature and extended holding time was aimed at effectively broadening the transition zone.[32] Typically, a homogenization temperature exceeding 1000°C is required for 17-4PH to attain complete supersaturation

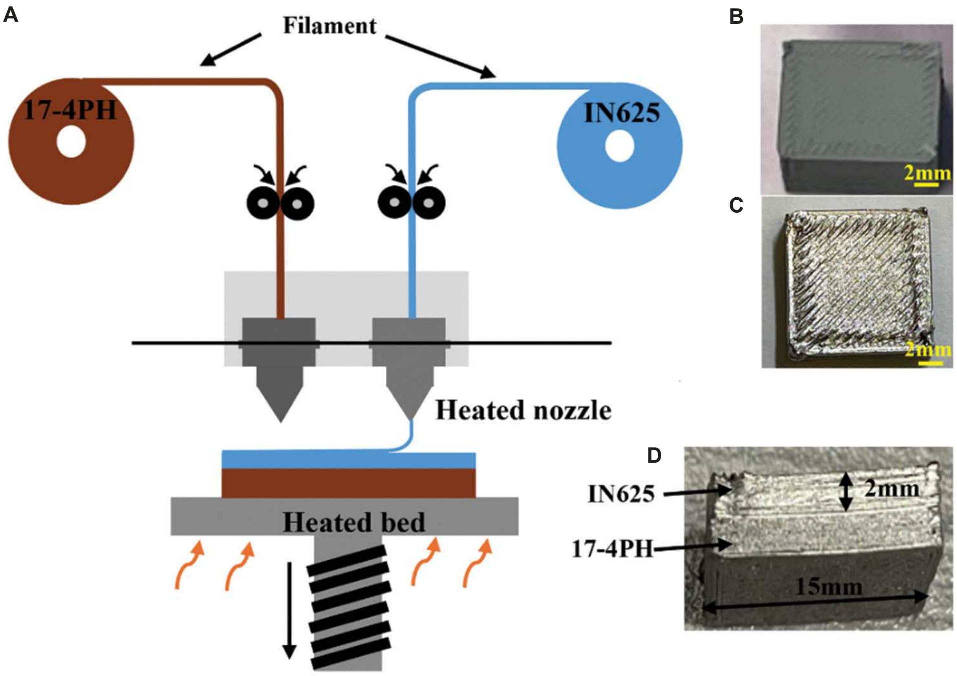

Figure 1. The illustration of the ES-AM process and the fabricated 17-4PH/IN625 bimetal part. (A) An illustration ES-AM process with a dual nozzle system (B) A bimetallic material after printing. (C) The top perspective of the sintered component. (D) Profile of the sintered component, showcasing geometrical details. Scale bars: 2 mm.
Abbreviation: ES-AM: Extrusion-based sintering-assisted additive manufacturing.

Table 1. Material properties for 17-4PH and IN625 filament and optimized printing parameters for 17-4PH/IN625 bimetallic green part

Parameters	17-4PH	IN625
Filament		
Version	V2	-
Diameter	1.75 mm	1.75 mm
Specification	400 cc/spool	200 cc/spool
Composition	20 vol.% wax, 20 vol.% polyethylene, and 60 vol.% powder	
Optimized printing parameters		
Nozzle temperature	230°C	210°C
Bed temperature	80°C	80°C
Chamber temperature	60°C	60°C
Nozzle size	0.4 mm	0.4 mm
Layer thickness	0.1 mm	0.1 mm
Infill density	100%	100%
Speed	40 mm/s	40 mm/s
Infill orientation	45°	135°

of martensite. Considering factors such as the presence of NbC and oxides, as well as the dimensions of prior austenite grain and martensite lath, the homogenization temperature was set at 1150°C to ensure adequate uniformity.[34] One of the recommended heat treatment procedures for the IN625 alloy involves subjecting it to a solutionizing operation at 1150°C. This thermal processing step serves to eliminate compositional inhomogeneities, eliminate secondary phases present, trigger recrystallization phenomena, and promote grain coarsening.[35] The aging temperature and duration were adjusted for specific applications to balance strength and toughness while controlling tempered martensite and precipitation. In addition, an aging heat treatment was employed (482°C for 1 h holding time), following HT8 to enhance hardness. Rapid cooling through water quenching was implemented for the samples to promote expedited heat extraction and mitigate the potential for carbide precipitation, especially within the temperature regime of 1150°C sustained for 8 h. Figure 2 illustrates the heat treatment conditions used during the experiments.

2.2. Microstructure characterizations and mechanical properties

To investigate the microstructure and microhardness, bimetallic samples were prepared in both as-sintered and heat-treated states. Pore distribution and grain morphology were analyzed using optical microscopy (OM; Olympus DSX 510, Olympus, Japan) and scanning electron microscopy (SEM; Supra 55-VP, Zeiss, Germany).

Table 2. The alloy composition of the 17-4PH and IN625 feedstocks

Weight %	Cr	Fe	Ni	Nb	Mo	Mn	Si	C	Cu	Co	Other elements
17-4PH	15 – 17.5	Balance	3 – 5	0.15 – 0.45	-	1	1	0.07	3 – 5	-	0.07
IN625	20 – 23	5	Balance	3.15 – 4.15	8 – 10	0.5	0.5	0.1	-	1	0.82

Table 3. Material properties of 17-4PH and IN625

Material properties	17-4PH V2	IN625
Relative density	>96.5%	>96.5%
Hardness (HRC)	36	7
Ultimate tensile strength (MPa)	1180	765
0.2% yield strength (MPa)	710	334
Elongation at break	7%	42%
Corrosion	Good	Excellent
Thermal coefficient	10.8×10^{-6}/°C[16]	12.8×10^{-6}/°C[17]

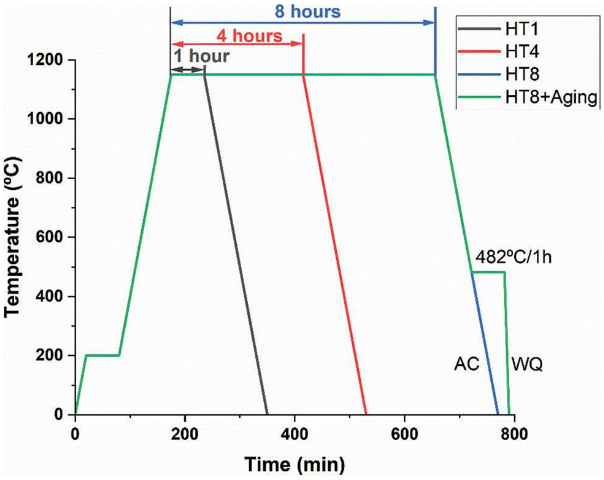

Figure 2. Schematic overview of heat treatment conditions. Abbreviations: AC: Air cooling; WQ: Water quenching.

Initially, the samples were sectioned transversely relative to the building direction and embedded in epoxy to ensure secure fixation. The process involved grinding and polishing, culminating in a final polish utilizing an alumina suspension with a particle size of 0.25 µm. After polishing, the samples underwent microstructural characterization utilizing an SEM integrated with an energy-dispersive X-ray spectroscopy (EDS) system to analyze the elemental distribution across the interfacial region. Meanwhile, internal porosity was assessed using OM at ×40 magnification, followed by the analysis of the polished internal surfaces of cut samples using ImageJ software (National Institutes of Health, USA). To reveal the grain structure, chemical etching was performed using Marble's and Kalling's 2 reagents (ES Laboratory, LCC, USA), followed by observation through OM. XRD analyses were employed to identify the phase constituents present in the bimetallic samples. Microindentation hardness testing following ASTM E384 guidelines was conducted utilizing a Vickers hardness tester (LM-310AT, LECO, USA). The test was conducted with a load of 1.0 kg, an approach speed of 60 µm/s, and a measurement period lasting 10 s.

3. Results and discussion

3.1. Interface characterization

The microstructure of the interface between 17-4PH and IN625 after heat treatment reveals metallurgical bonding, as depicted in Figure 3. Figure 3A-D depicts the variation in pore population and dimensions across the polished surface subjected to distinct heat treatment conditions. The grain morphology of 17-4PH after surface etching with Marble's reagent is presented in Figure 3A1-D1. Small pores (dark pores) were distributed within the 17-4PH parts due to insufficient densification when employing the sintering profiles for IN625. Nevertheless, with an increase in holding time, the pore size decreased owing to the heat contribution facilitating densification to a certain extent.[36] Typical martensitic and ferrite phases were observed on the 17-4PH side of the interface, resulting from the precipitation hardening process.[37] Concurrently, the grain size of 17-4PH initially decreased and subsequently increased with increasing holding time, a phenomenon attributable to recrystallization and grain growth induced by excessive heat input.[32] The chemical etching process did not reveal the phase composition of IN625; however, subsequent XRD analysis confirmed the presence of the austenitic phase, corroborating the findings reported in the literature.[38]

No evident intermetallic phases were formed at the interface under different heat treatment conditions, which aligns with the findings in the relevant literature.[5] In Figure 3A-D, the interface is marked by a band with a lighter appearance, which lacks visible grain structure, suggesting an absence of grain development in this transition zone. Figure 3 illustrates that the thickness of the interfacial white bands did not significantly vary with extended holding times, maintaining an approximate width of 60 µm in both as-sintered and heat-treated states. Significantly, the precipitation of minute particulates, visible as black dots in Figure 3, was localized within the IN625 alloy region. Meanwhile, as time increases, the porosity of the entire part decreases, as depicted in Figure 4, which uses images from OM taken at three different locations along the interface.

SEM analysis revealed a comparable phenomenon occurring at the interface, irrespective of whether heat treatment was applied or not, as shown in Figure 4. To

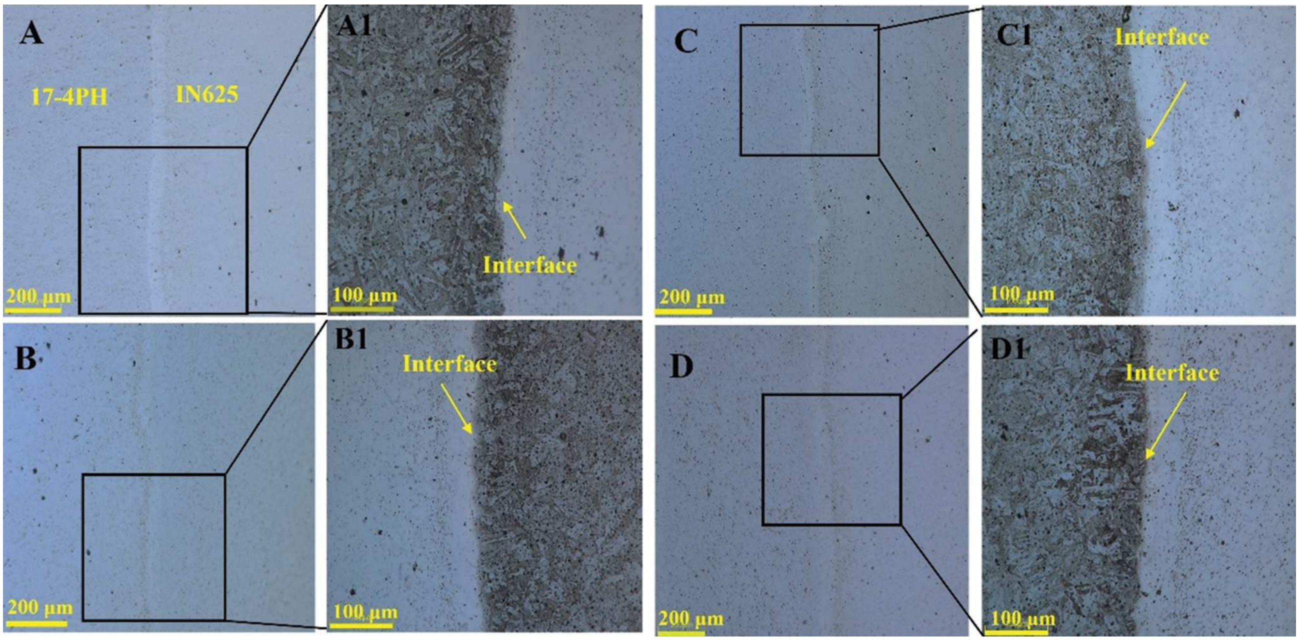

Figure 3. Optical micrographs of the bimetallic part at different dwell times. (A) 1 h, (B) 4 h, (C) 8 h, and (D) 8 h + aging, all at 482°C/h. Scale bars: 200 μm; magnification: ×222. The enlarged images (A1, B1, C1, and D1) represent chemically etched surfaces after polishing. Scale bars: 100 μm; magnification: ×555.

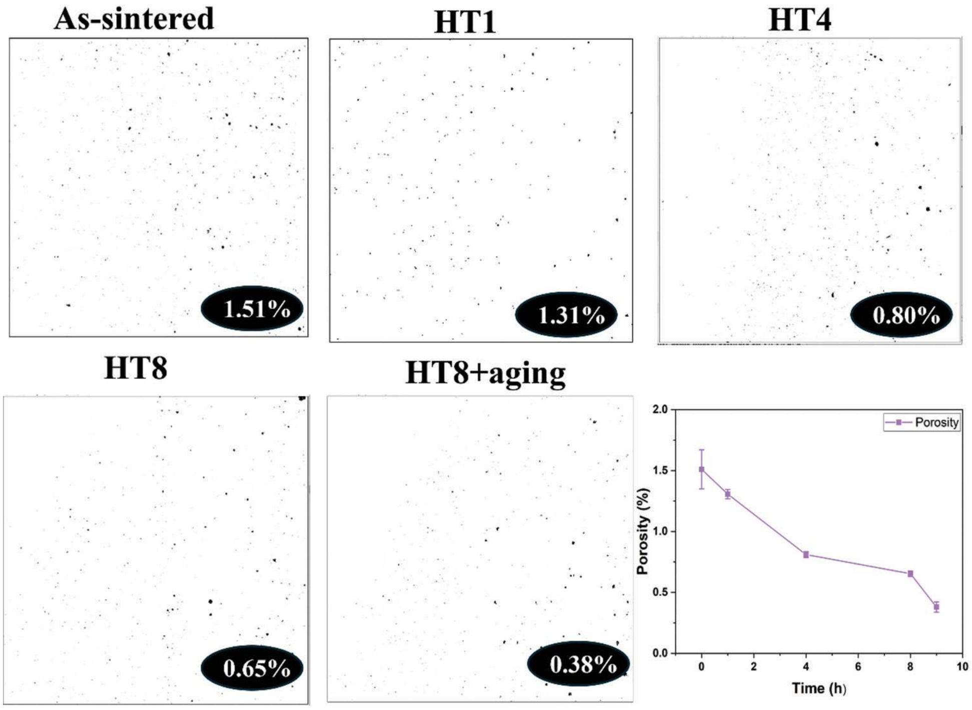

Figure 4. Internal porosity of samples at different heat treatment conditions.
Note: Images were processed using ImageJ software.

further delineate the specific transition zone within the interface, an EDS line scan analysis was conducted to investigate the elemental variations. The EDS line scan data, as depicted in Figure 5F, reveal that the white bands observed in the OM images (Figure 3) and the precipitate accumulations (Figure 5A-E) correspond to regions where iron (Fe) and Ni constituents undergo interdiffusion in opposite directions. Within these areas, the concentrations of Fe and Ni elements are diminished in comparison to their respective pure forms, accompanied by a depletion of Nb and Mo relative to pure Inconel. Conversely, Cr exhibits a uniform distribution since both 17-4PH and IN625 alloys contain this element.

These white bands are characterized by reduced porosity, exhibiting either smaller pores or an absence of pores altogether, as evident from Figure 5A-E. The white band region, dominated by the Fe element, is referred to as the Fe-predominant zone. With increasing holding time, the thickness of these bands remains relatively unchanged, a phenomenon vividly illustrated in Figure 3. It measures almost 60 μm under both as-sintered and heat-treated conditions, consistent with our previous research.[39] Another region is primarily characterized by Ni elements, termed the Ni-predominant zone, as illustrated in Figure 5F. The segregation of precipitates and inclusions within this region undergoes modifications as the holding time increases. During heat treatment, precipitates form during heat treatment as carbon diffuses from steel into the Inconel alloy, containing elements (Cr, Mo, Nb) with a strong affinity for carbon.[40] After 1 h of heat treatment, the size and distribution of precipitates and inclusions diminish in comparison to the as-sintered condition. Similarly, the 4-h holding time yields the smallest precipitates and inclusions relative to the other holding times investigated. However, an excessively prolonged holding time of 8 h promotes grain growth, resulting in larger precipitate sizes. In addition, elongated precipitates are observed in the sample subjected to the 8-h holding time.

3.2. Element diffusion at the interface

The behavior of element diffusion at the interface between 17-4PH and IN625 is critical for the bonding quality and strength of the bimetallic composite. Previous observations indicate that a larger distance of alloy diffusion correlates with increased interfacial shear strength.[32,41] This study highlights significant variations in the chemical compositions of 17-4PH and IN625, particularly in the elements Fe, Ni, Mo, and Nb. These variations in elemental concentrations between two materials initiate diffusion during heat treatments, detectable through EDS analysis. SEM images and EDS maps illustrating the distribution of Fe and Ni elements near the interface post-annealing at varied durations of 1, 4, and 8 h are presented in Figure 6.

The primary constituents of the diffusion zone, Fe and Ni, exhibit marked variations in their concentrations within this region. Notably, the concentration of Ni sharply

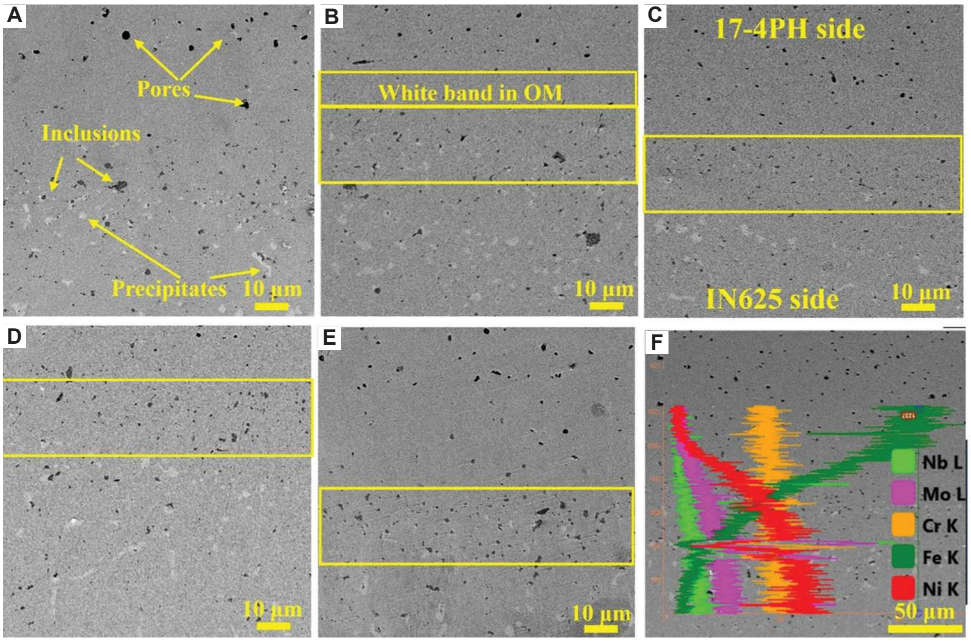

Figure 5. Scanning electron microscopy analysis of the interface following different heat treatment conditions. (A) As-sintered; (B) heat-treated at 1150°C for 1 h; (C) 4 h; (D) 8 h; (E) 8 h + aging; and (F) energy-dispersive X-ray spectroscopy line scanning of the interface highlighting five primary elements. Scale bars: (A-E) 10 μm, magnification: ×1280; (F) 50 μm, magnification: ×862.
Note: In all panels, the top part is the 17-4PH side, and the bottom part is the IN625 side. Abbreviation: OM: Optical microscopy.

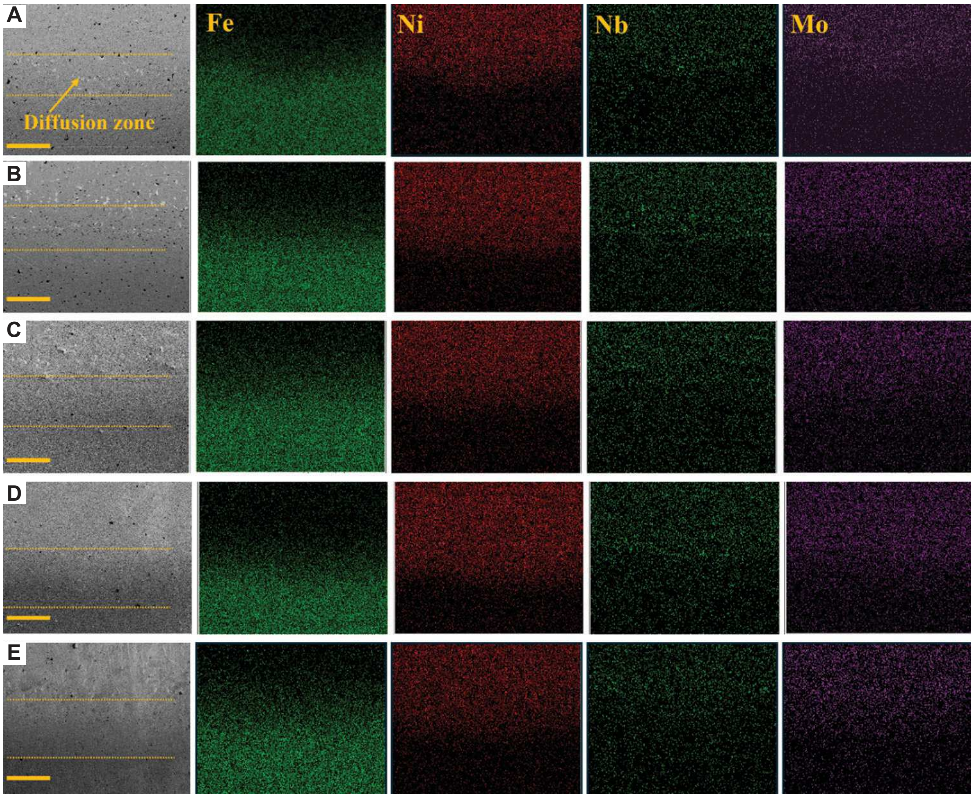

Figure 6. Scanning electron microscopic images and energy-dispersive X-ray spectroscopy maps of Fe, Ni, Nb, and Mo adjacent to the interface following different annealing durations. (A) As-sintered; (B) 1 h; (C) 4 h; (D) 8 h; and (E) 8 h + aging at 482°C for 1 h. Scale bars: 100 µm, magnification: ×543).

declines at the boundary of the diffusion zone, while that of Fe correspondingly surges. In the diffusion zone between two layers, the boundary of Ni and Fe elements is not distinct after 1 h and 4 h, as shown in Figure 6; however, a gradient distribution of these elements becomes noticeable after 8 h. In addition, Nb and Mo elements segregate near the diffusion zone, leading to the formation of delta phase or precipitates in IN625, which is characterized by increased brittleness, consistent with another previous publication.[42] Furthermore, the Nb- and Mo-rich zone, depicted in Figure 6A as a light area, becomes less pronounced and diminishes in size as the holding time is extended.

To measure the diffusion distance of the alloy, profile curves depicting the diffusion of elements in various states (Figure 7A-E) were plotted along the scan line shown in Figure 7. The transition zone for diffusion between the two steel layers expands as the holding time is prolonged. This result is aligned with the findings reported by Li *et al.*[32] and Jiang *et al.*,[43] who noted a similar trend. The expansion of the transition zone is believed to follow a parabolic law, allowing its thickness to be quantified as Equation I:

$$\delta = \sqrt{K_0 \exp\left(\frac{-Q}{RT}\right) * t} \qquad \text{(I)}$$

where δ denotes the thickness (m), t stands for annealing duration (s), K_0 represents the factor (m^2/s), Q signifies the activation energy (J·mol) required for interface diffusion, R is the universal gas constant (8.3145 J/(mol·k)), and T indicates the absolute temperature (Kelvin).

Figure 7 presents the EDS line scanning across the interfaces of 17-4PH/IN625 bimetals fabricated under varying solution times. It reveals distinct concentrations of Fe and Cr elements at the interfaces, indicating a high-quality metallurgical bond. In addition, it demonstrates that the thickness of the reaction layer significantly increases with extended heat treatment times, correlating with related research on diffusion zone thickness.[43] Initially, a 1-h solution time slightly thickens the reaction layer compared to the as-sintered state, with the diffusion zone measuring 105 µm compared to 75 µm for the as-sintered sample, as shown in Figure 7A. Extending the solution time to 4 h results in the reaction layer thickening to approximately 160 µm, a 52% increase over the 1-h solution time sample, as detailed in Figure 7B. Nevertheless, there are holes within the reaction layer. According to Equation I, $\delta_3 = \sqrt{2}\,\delta_2 = 2\sqrt{2}\,\delta_1$, where δ_1, δ_2, δ_3 represent the diffusion zone thicknesses under heat treatment for 1, 4, and 8 h, respectively. At an 8-h solution time in Figure 7C, the transition zone reaches nearly 220 µm,

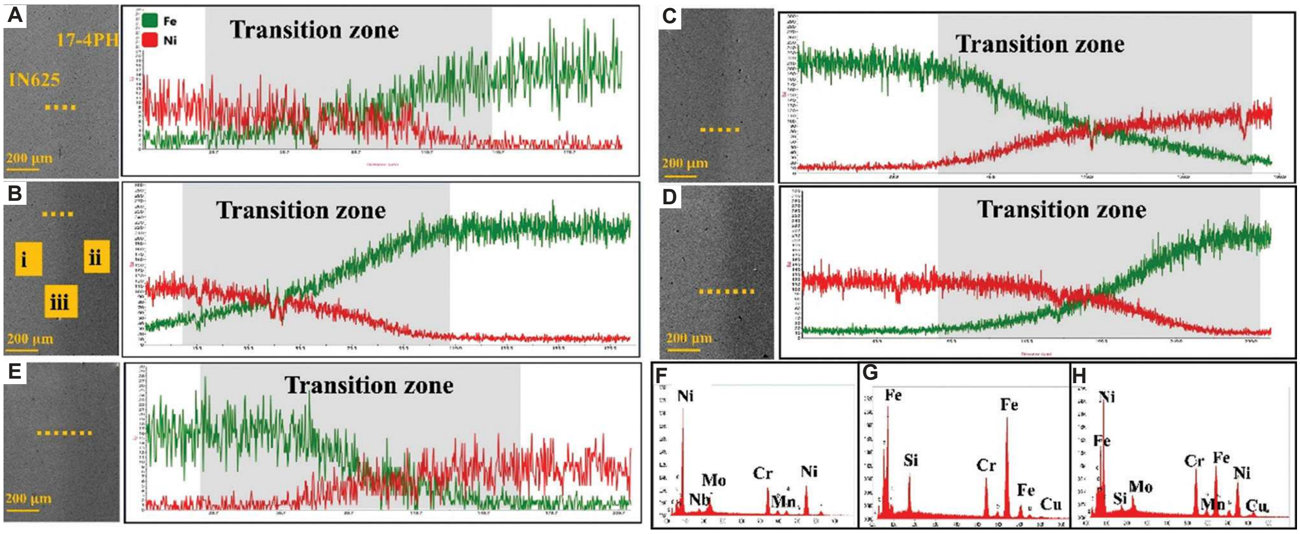

Figure 7. Scanning electron microscopic images and transition zones across different heat treatment conditions. (A) As-sintered; (B) treated at 1150°C for 1 h; (C) 4 h; (D) 8 h; and (E) 8 h + aging. Scale bars: 200 µm, magnification: ×200. Elemental composition analysis at specific locations in (B): (F) Element at point A, (J) element at point B, and (K) element at point C.

about 2.1 times the thickness at 1 h, aligning closely with the calculated value of approximately 2.8 times. Prolonged solution times, while increasing the reaction layer thickness, also enhance the risk of cracking and excessive growth of grain size, as shown in Figure 3. Additional EDS analyses at the interfaces of 17-4PH/IN625 bimetals for different solution times, as illustrated in Figure 7, indicate that solution time does not alter the composition of interface phases within the reaction layer. In addition, Figure 7F and G present EDS point scan analyses at points i and ii in Figure 7B, corresponding to the 17-4PH and IN625 alloys, respectively. Figure 7H illustrates elemental distribution at point iii in Figure 7B, identifying Fe, Ni, Co, Si, and Mn in the specified area.

3.3. Interface microstructure analysis

To delve deeper into the characteristics of the diffusion zone, a focused examination of a select region was conducted to analyze the distribution of elements and identify the presence of precipitates, as illustrated in Figure 8. This investigation employed linear analysis and mapping techniques to scrutinize the chemical composition of the white band observed in Figure 3 and the precipitates found within the diffusion zone.

Figure 8A illustrates the characteristic structure observed at the interface, which features a black zone encircled by a lighter zone. Elemental mapping reveals that the darker oxides are composed of oxygen (O), manganese (Mn), and Cr, while Nb and Mo constitute the lighter secondary phase. These zones are characterized as Ni-predominant areas, as corroborated by EDS analyses referenced in Figure 8A, C, and E. Furthermore, examination of Figure 8F and J reveals that the Fe-predominant zone comprises Fe, Cr, and Mn elements exclusively, devoid of any other discernible phases, thus aligning with earlier findings outlined in Section 3.1.

The emergence of oxidized regions and the formation of carbides are anticipated outcomes during the debinding and sintering stages, largely attributable to the accumulation of impurities. Within the comprehensive microstructure of the material, carbides, characterized by a blocky appearance, were observed both internally and at the grain boundaries in parts manufactured through ES-AM.[4] Further SEM analyses highlighted a homogeneously distributed secondary phase within the material (Figure 7A, B, and D), which was predominantly composed of Mo, Nb, and Si (Figure 7B). A comparative analysis of its EDS spectrum with that of the matrix revealed a marginal increase in carbon content within this secondary phase, which also exhibited a reduction in Ni, Fe, and Cr in comparison to the matrix, as outlined in Table 4. Heat-treated samples, as contrasted with as-sintered ones, demonstrated the presence of elongated carbides, as illustrated in Figure 3. These carbides were arranged in semi-continuous sequences along the grain boundaries, consistent with the literature.[35] In other studies, a similar phenomenon was observed in heat-treated IN625 produced using PBF and DED methods.[44] These carbides are classified into two types: NbC and Cr23C7.[45] Among the two, NbC typically has a higher dissolution temperature (above 1200°C) and remains incompletely dissolved during heat treatment under 1150°C.[29] Cr23C7 usually forms during the solid-phase transition process due to a

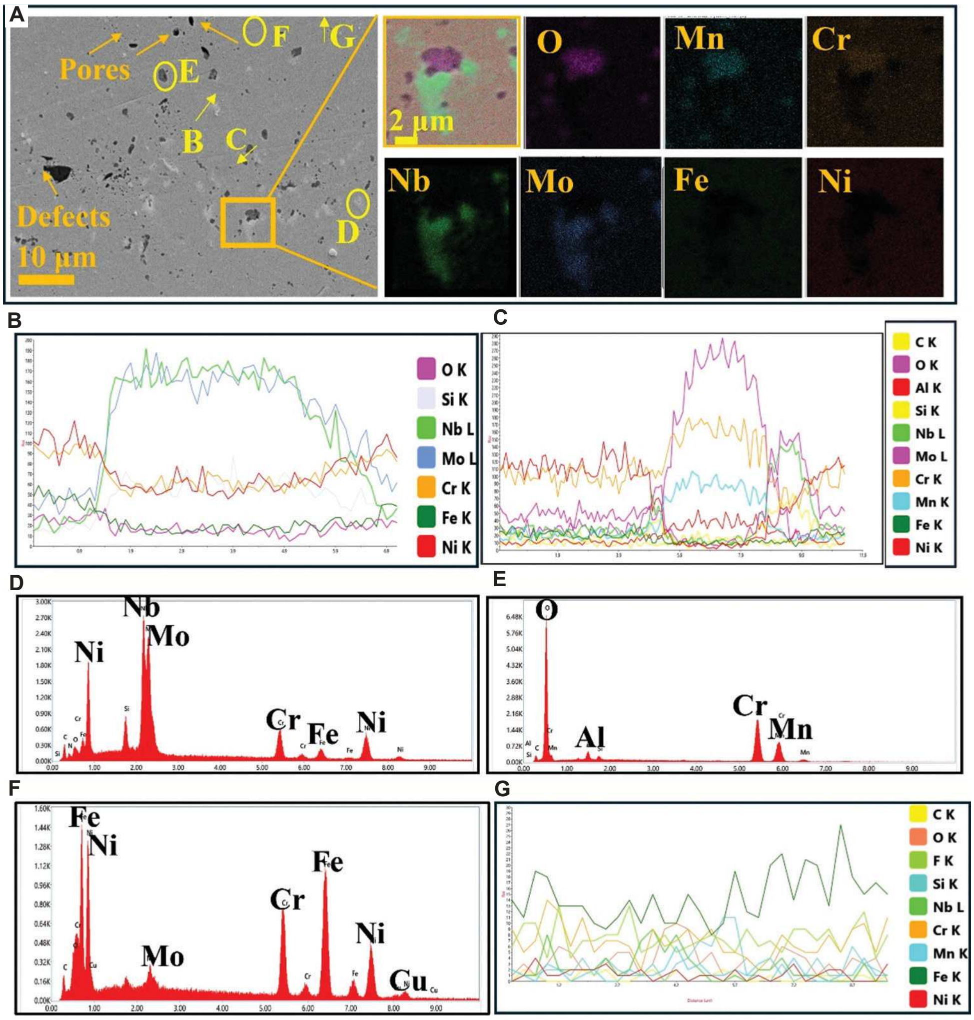

Figure 8. Microstructural analysis of interfaces. (A) Elemental mapping covering an oxide inclusion and secondary phase. Scale bars: 10 μm, magnification: ×3678; Scale bars: 2 μm, magnification: ×3678. Energy-dispersive X-ray spectroscopy (EDS) line scans for light (B) and dark (C) areas; elemental analyses for specific spots: (D) analysis at spot D, (E) analysis at spot E; (H) EDS line scans for white band.

Table 4. Element distribution in the interface of bimetal

Weight %	Cr	Fe	Ni	Nb	Mo	Mn	Si	C	O
Precipitates	9.7	5.1	20.9	25.8	15.9	-	2.1	16.5	2.3
Oxides	39.5	-	-	-	-	19.5	0.5	8.7	30.4
White bands	14.8	51.9	14.6	-	1.4	-	0.3	10.6	-
17-4PH	12.6	57.6	3.1	-	-	0.4	2.8	9.1	7.0
IN625	18.5	5.8	52.0	2.6	7.0	-	0.6	11.6	1.9

slower cooling rate.[46] The elongated morphology of these carbides is due to the slow cooling rates experienced at the conclusion of the heat treatment process, a detail that aligns with the observed structural characteristics.

The XRD patterns of phases present at the 17-4PH/IN625 composite, both in as-sintered and heat-treated states, were analyzed to assess changes in intermetallic phases, as depicted in Figure 9A. The primary phases in 17-4PH are the α-phase (martensitic and ferritic phases), whereas in IN625, the dominant phase is the γ-phase (austenitic phase). No additional phases were discovered following the heat treatments, which were under 1150°C for various durations, with or without subsequent aging, of 17-4PH, with only austenite and martensite peaks detected.[20] Both direct aging and aging following Hot Isostatic Pressing (HIP) of 17-4PH fabricated through PBF showed no formation of other phases.[31,47] Furthermore, the absence of additional peaks suggests the absence of reactive phase formation within the bimetallic structure of SS316L and IN718 alloy.[48] Similarly, further XRD patterns corroborate the observation in our research that no new intermetallic phases form within the diffusion zone following heat treatment, aligning with the findings from EDS analyses. Independent of

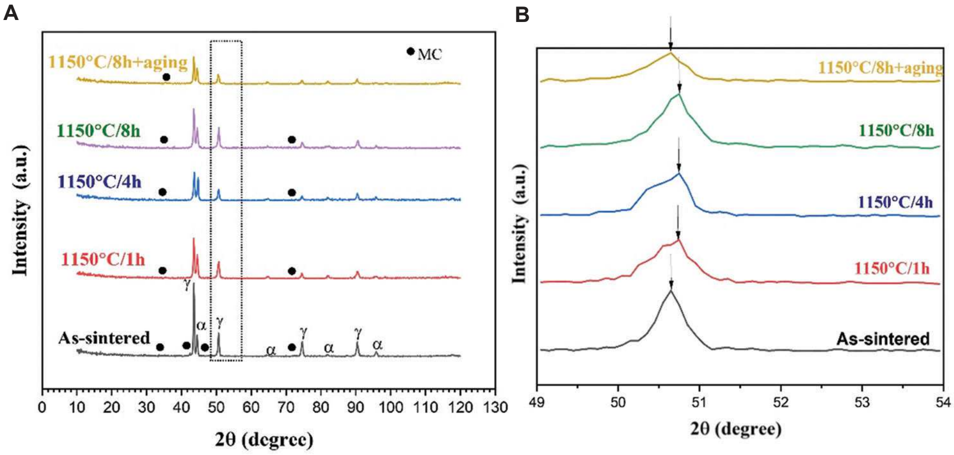

Figure 9. The X-ray diffraction (XRD) patterns of 17-4PH/IN625 bimetallic samples under different heat treatment conditions: (A) Overall XRD patterns; (B) The XRD peak shift at specific location. (A) The XRD patterns and (B) the XRD peak shift at the specific locations of 17-4PH/IN625 bimetallic samples under different treatment conditions.

whether they underwent heat treatment, the reaction layers predominantly consist of oxides and precipitates exhibiting a high concentration of Nb and Mo elements. In addition to the Ni matrix, peaks indicative of MC carbides were also identified.[49] Similarly, MC carbides were found in IN625 treated under 1150°C.[50] The heat treatment process appears to diminish the presence of carbides, as evidenced by Figure 4, showing a reduction in both the size and quantity of carbides. Simultaneously, as the duration increases, the peak position shifts due to stress relaxation and precipitate formation,[35] as depicted in Figure 9B. As IN625 alloy and 17-4PH possess different coefficients of thermal expansion, the stress level escalates with prolonged time. Previous literature has reported similar observations regarding the behavior of IN625 under various heat treatment conditions, especially when compared to stress-free powder materials.[50]

3.4. Effects of heat treatment on microhardness

The impact of heat treatment on the microhardness of 17-4PH/IN625 bimetallic parts was determined through microhardness testing. Figure 10 presents the microhardness distributions along the bimetallic interfaces under both as-sintered and heat-treated states.

The microhardness of the bimetal improves uniformly across all areas, including both the 17-4PH side and the IN625 side, as well as the interface, after undergoing heat treatment. In the case of 17-4PH steel, there is an initial increase in hardness, peaking at 367 $HV_{1.0}$, followed by a subsequent decline. This observation aligns with other studies wherein a peak hardness value of approximately 360 $HV_{1.0}$ was noted following solution heat treatment.[34] The enhancement in hardness can be attributed to the reduction in porosity and the diminution of pore size. However, over time, an enlargement in grain size is discernible, as indicated in Figure 3, adversely affecting hardness. The predominant phases in 17-4PH consist of ferrite and martensite. Slower cooling rates or extended heating periods facilitate the migration of carbon and other alloying elements, leading to a reversal from martensite to ferrite. An increase in the proportion of ferrite, at the expense of martensite, typically results in a diminished hardness, given the inherent softness of ferrite compared to martensite.[51] A comparable trend was observed in the microhardness of 17-4PH manufactured through PBF as time progressed, manifesting a decrease. This trend is attributed to the presence of samples consisting of fine lath martensite lacking distinct preferred orientations, coupled with the elimination of delta-ferrite following homogenization.[34] Meanwhile, through aging followed by homogenization, fine particles (precipitates) form and impede dislocation movement, thereby augmenting hardness compared to the material devoid of aging, as illustrated in Figure 10. For IN625, the microhardness initially experiences a marginal increase from 208 $HV_{1.0}$ to 209 $HV_{1.0}$, before subsequently decreasing to 205 $HV_{1.0}$. The strengthening of IN625 alloy mainly ensues through solid solution hardening facilitated by Cr, Mo, and Nb.[49] However, during heat treatment, the segregation of these elements within the transition zone forms precipitates, thereby reducing the strengthening effect in IN625. In alternative bimetallic structures consisting of IN625 and Ti6Al4V, the absence of Cr- and Mo-enriched phases within the Ni matrix on the IN625 side culminates in a reduced hardness gradient.[52] With prolonged holding time, the enlargement of

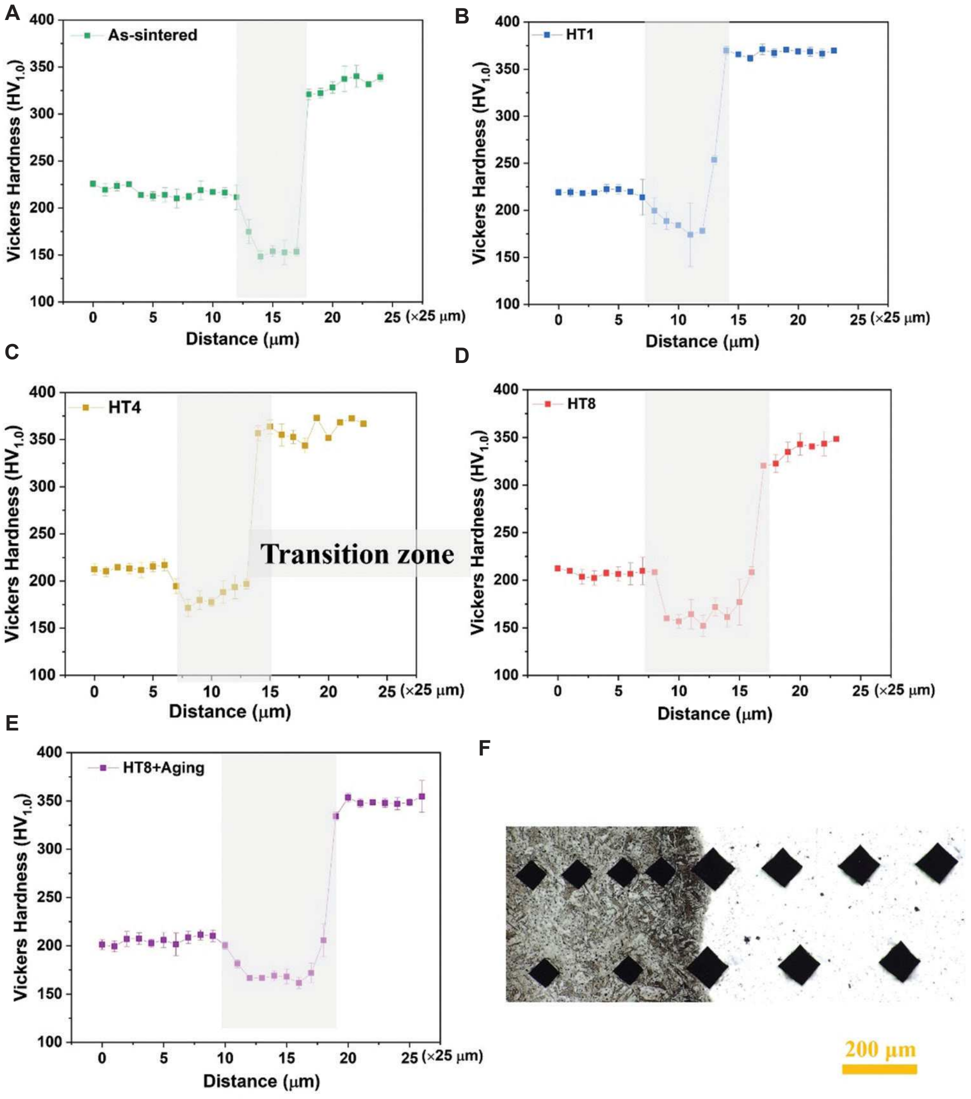

Figure 10. Microhardness profiles across bimetal interfaces. (A) As-sintered and heat-treated at 1150°C for (B) 1 h, (C) 4 h, (D) 8 h, and (E) 8 h + aging. (F) Optical microscopic image showing indentations. Scale bar: 200 μm; magnification: ×264.

Table 5. Thickness of the diffusion zone across various treatment conditions

Diffusion zone (μm)	As-sintered	HT1	HT4	HT8	HT8+aging
EDS line scan analysis (μm)	75	105	160	220	200
Results derived from Equation I	-	a	2 a	2.8 a	2.8 a
Microhardness measurements (μm)	100	150	188	250	250

Abbreviation: EDS: Energy-dispersive X-ray spectroscopy.

grain size and the reduction in the spread of elongated precipitates on the IN625 side (Figure 5) lead to reduced microhardness.

The microhardness distributions, regardless of whether in the as-sintered or heat-treated state, exhibit a consistent pattern, wherein the microhardness of the reaction layers is markedly lower than that of the matrices, particularly evident in the steel matrix, as depicted in Figure 10. The indentations on the interface appear larger compared to those in Inconel alloy and SS, as depicted in Figure 10F. This significant decrease in microhardness within the diffusion zone is attributed to the presence of pores and the absence of secondary phases.

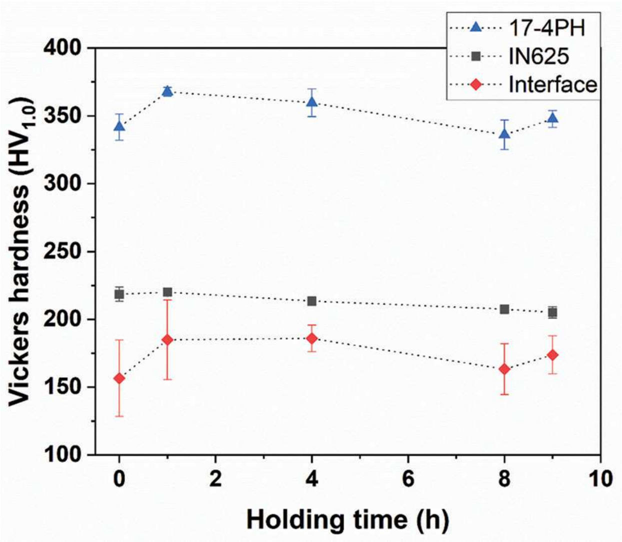

Figure 11. Microhardness changes along the bimetallic interfaces under various conditions.

With an increase in holding time, the microhardness of the transition zone initially rises, and then decreases after 4 h, as shown in Figure 11. Heat treatment for 4 h yields the highest microhardness value, approximately 186 $HV_{1.0}$, compared to the lowest value of 156 $HV_{1.0}$ observed in samples without heat treatment. This observed increase represents a nearly 20% post-treatment enhancement, closely aligning with the microhardness on the IN625 side. With the increase in time, the size of pores reduces, and the occurrence of pores decreases. During heat treatment, oxides and carbides form in the transition zone, creating an intermetallic compound that is both hard and brittle. Excessively long dwell times typically result in larger grain sizes, which are detrimental to the hardness of the interface. Notably, microhardness measurements also allow us to determine the thickness of the transition zone in Figure 10A-D. These values are consistent with results calculated using Equation I and EDS scan line analysis results from Table 5.

4. Conclusion

This study investigated the effects of various heat treatment approaches on the microstructure and mechanical properties of 17-4PH/IN625 bimetallic components fabricated through the ES-AM process. The key findings are summarized below.

(i) The 17-4PH/IN625 bimetallic composite exhibited excellent interfacial bonding after heat treatment, with few pores at the interface and uniform elemental distribution without delamination. The diffusion zone could be separated into two regions: an Fe-rich zone and a Ni-rich zone (containing oxides and Mo-, Nb-rich precipitates). Significant Nb segregation was observed in the transition zone.

(ii) With extended dwell time, overall porosity decreased. Simultaneously, carbides, an intermetallic compound (a hard and brittle phase), exhibited a more uniform and finer distribution after 4 h of heat treatment.

(iii) The thickness of the transition zone increased with prolonged dwell times, resulting in enhanced bonding strength for the bimetallic components. Empirical data on microhardness and the theoretical parabolic diffusion law provided supporting evidence for the observed phenomenon.

(iv) No new phases were detected after heat treatment; however, XRD peak shifts occurred due to stress relaxation and precipitate formation.

(v) The microhardness of the transition zone increased with heat treatment, reaching a maximum of 186 $HV_{1.0}$ after a 4-h holding time. The optimized heat treatment condition was determined to be 1150°C for 4 h to attain uniform microstructures and high bonding strength.

Future studies could involve complementary computational efforts involving modeling and simulations to acquire insights into the mechanisms facilitating interfacial bonding. Particular attention should be paid to elucidating the role of elemental segregation and diffusion phenomena.

Acknowledgments

The authors extend their sincere gratitude to the anonymous reviewers for their valuable comments and suggestions, which have greatly contributed to the improvement of this paper. This work was funded by the United States National Science Foundation through the award CMMI-2224309.

Funding

This work was funded by the United States National Science Foundation through the award CMMI-2224309.

Conflict of interest

The authors declare that they have no competing interests.

Author contributions

Conceptualization: Yulin Liu and Fuda Ning
Formal analysis: Yulin Liu and Dayue Jiang
Investigation: Yulin Liu
Methodology: Yulin Liu and Dayue Jiang
Writing – original draft: Yulin Liu
Writing – review & editing: All authors
All authors have read and agreed to the published version of the manuscript.

Ethics approval and consent to participate

Not applicable.

Consent for publication

Not applicable.

Availability of data

Data are available from the corresponding author on reasonable request.

References

1. Bandyopadhyay A, Zhang Y, Onuike B. Additive manufacturing of bimetallic structures. *Virtual Phys Prototyp.* 2022;17(2):256-294.

   doi: 10.1080/17452759.2022.2040738

2. Zhang B, Zhang W, Xiao H, Yang H, Wang Y, Chen B. QCr0. 8 Cu alloy/S06 stainless steel bimetal structure via In718 multi-interlayer fabricated by laser powder hybrid additive manufacturing. *J Mater Res Technol.* 2023;24:1034-1042.

   doi: 10.1016/j.jmrt.2023.03.073

3. Jiménez A, Bidare P, Hassanin H, Tarlochan F, Dimov S, Essa K. Powder-based laser hybrid additive manufacturing of metals: A review. *Int J Adv Manuf Technol.* 2021;114:63-96.

   doi: 10.1007/s00170-021-06855-4

4. Sahasrabudhe H, Harrison R, Carpenter C, Bandyopadhyay A. Stainless steel to titanium bimetallic structure using LENS^{TM}. *Addit Manuf.* 2015;5:1-8.

   doi: 10.1016/j.addma.2014.10.002

5. Wu H, Xie X, Liu S, *et al*. Bonding behavior of Bi-metal-deposits produced by hybrid cold spray additive manufacturing. *J Mater Process Technol.* 2022;299:117375.

   doi: 10.1016/j.jmatprotec.2021.117375

6. Jiang D, Ning F. Physical-mechanical behaviors of stainless steel plate-lattice built by material extrusion additive manufacturing. *J Mater Process Technol.* 2022;309:117739.

   doi: 10.1016/j.jmatprotec.2022.117739

7. Jiang D, Ning F. Reprint of: Bi-metal structures fabricated by extrusion-based sintering-assisted additive manufacturing. *J Manuf Process*. 2023;100:20-26.

   doi: 10.1016/j.jmapro.2023.05.101

8. Zhang Y, Bandyopadhyay A. Influence of compositionally graded interface on microstructure and compressive deformation of 316L stainless steel to Al12Si aluminum alloy bimetallic structures. *ACS Appl Mater Interfaces.* 2021;13(7):9174-9185.

   doi: 10.1021/acsami.0c21478

9. Wei C, Liu L, Gu Y, *et al*. Multi-material additive-manufacturing of tungsten-copper alloy bimetallic structure with a stainless-steel interlayer and associated bonding mechanisms. *Addit Manuf.* 2022;50:102574.

   doi: 10.1016/j.addma.2021.102574

10. Ergene B, Yalçın B. Investigation on mechanical performances of various cellular structures produced with fused deposition modeling (FDM). *J Fac Eng Archit Gazi Univ*. 2023;38:201-207.

    doi: 10.17341/gazimmfd.945650

11. Mousapour M, Salmi M, Klemettinen L, Partanen J. Feasibility study of producing multi-metal parts by Fused Filament Fabrication (FFF) technique. *J Manuf Process*. 2021;67:438-446.

    doi: 10.1016/j.jmapro.2021.05.021

12. Seleznev M, Roy-Mayhew JD. Bi-metal composite material for plastic injection molding tooling applications via fused filament fabrication process. *Addit Manuf.* 2021;48:102375.

    doi:10.1016/j.addma.2021.102375

13. Sun Y, Hebert RJ, Aindow M. Effect of heat treatments on microstructural evolution of additively manufactured and wrought 17-4PH stainless steel. *Mater Des*. 2018;156:429-440.

    doi: 10.1016/j.matdes.2018.07.015

14. Karmuhilan M, Kumanan S. A review on additive manufacturing processes of inconel 625. *J Mater Eng Perform*. 2021;31:2583-2592.

    doi: 10.1007/s11665-021-06427-3

15. Jagtap BM, Kakandikar GM, Jawade SA. Mechanical behavior of inconel 625 and 17-4 PH stainless steel processed by atomic diffusion additive manufacturing. In: Dave HK, Dixit US, Nedelcu D, editors. *Recent Advances in Manufacturing Processes and Systems*. Berlin: Springer Nature Singapore; 2022. p. 583-594.

    doi: 10.1007/978-981-16-7787-8

16. Mattli MR, Khan A, Matli PR, *et al*. Effect of Inconel625 particles on the microstructural, mechanical, and thermal properties of Al-Inconel625 composites. *Mater Today Commun*. 2020;25:101564.

    doi: 10.1016/j.mtcomm.2020.101564

17. Dash A, Bandyopadhyay A. 17-4 PH and SS316L bimetallic structures via additive manufacturing. *Virtual Phys Prototyp.* 2024;19(1):e2292695.

    doi: 10.1080/17452759.2023.2292695

18. Du Plessis A, Razavi N, Benedetti M, *et al*. Properties and applications of additively manufactured metallic cellular materials: A review. *Prog Mater Sci*. 2022;125:100918.

    doi: 10.1016/j.pmatsci.2021.100918

19. Li G, Jiang W, Guan F, Zhu J, Yu Y, Fan Z. Effect of different Ni interlayers on interfacial microstructure and bonding properties of Al/Mg bimetal using a novel compound casting. *J Manuf Process*. 2020;50:614-628.

    doi: 10.1016/j.jmapro.2020.01.017

20. Wu B, Qiu Z, Pan Z, *et al*. Enhanced interface strength in

steel-nickel bimetallic component fabricated using wire arc additive manufacturing with interweaving deposition strategy. *J Mater Sci Technol*. 2020;52:226-234.

doi: 10.1016/j.jmst.2020.04.019

21. Li P, Gong Y, Xu Y, Qi Y, Sun Y, Zhang H. Inconel-steel functionally bimetal materials by hybrid directed energy deposition and thermal milling: Microstructure and mechanical properties. *Arch Civ Mech Eng*. 2019;19:820-831.

doi: 10.1016/j.acme.2019.03.002

22. Dang X, Li Y, Chen K, Luo S, Liang X, He W. Insight into the interfacial architecture of a hybrid additively-manufactured stainless steel/Ni-based superalloy bimetal. *Mater Des*. 2022;216:110595.

doi: 10.1016/j.matdes.2022.110595

23. Chen N, Khan HA, Wan Z, *et al*. Microstructural characteristics and crack formation in additively manufactured bimetal material of 316L stainless steel and Inconel 625. *Addit Manuf*. 2020;32:101037.

doi: 10.1016/j.addma.2020.101037

24. Fan H, Shi Q, Wang C, Tian Y, Zhou K, Yang S. Laser powder bed fusion of bimetallic stainless steel/Nickel-based superalloy: Interface and mechanical properties. *Mater Sci Eng A*. 2023;877:145193.

doi: 10.1016/j.msea.2023.145193

25. Ferro P, Fabrizi A, Elsayed H, Berto F, Savio G. Creating IN718-high carbon steel Bi-metallic parts by fused deposition modeling and sintering. *Procedia Struct Integr*. 2023;47:535-544.

doi: 10.1016/j.prostr.2023.07.071

26. Ahsan MR, Fan X, Seo GJ, *et al*. Microstructures and mechanical behavior of the bimetallic additively-manufactured structure (BAMS) of austenitic stainless steel and Inconel 625. *J Mater Sci Technol*. 2021;74:176-188.

doi: 10.1016/j.jmst.2020.10.001

27. Kosturek R, Wachowski M, Śnieżek L, Gloc M. The influence of the post-weld heat treatment on the microstructure of inconel 625/carbon steel bimetal joint obtained by explosive welding. *Metals*. 2019;9(2):246.

doi: 10.3390/met9020246

28. Gope DK, Chattopadhyaya S. Dissimilar welding of nickel based superalloy with stainless steel: Influence of post weld heat treatment. *Mater Manuf Process*. 2022;37(2):136-142.

doi: 10.1080/10426914.2021.1945095

29. Liu J, Miao Y, Wang Z, Zhao Y, Wu Y, Li C. Effect of heat treatment on microstructure and properties of additively manufactured aluminum bronze-steel bimetallic structures. *Mater Charact*. 2024;207:113462.

doi: 10.1016/j.matchar.2023.113462

30. Miriyev A, Levy A, Kalabukhov S, Frage N. Interface evolution and shear strength of Al/Ti bi-metals processed by a spark plasma sintering (SPS) apparatus. *J Alloys Compd*. 2016;678:329-336.

doi: 10.1016/j.jallcom.2016.03.137

31. Wang Y, Song R, Yanagimoto J, Li H. Effect of heat treatment on bonding mechanism and mechanical properties of high strength Cu/Al/Cu clad composite. *J Alloys Compd*. 2019;801:573-580.

doi: 10.1016/j.jallcom.2019.06.132

32. Li Z, Zhao J, Jia F, *et al*. Interfacial characteristics and mechanical properties of duplex stainless steel bimetal composite by heat treatment. *Mater Sci Eng A*. 2020;787:139513.

doi: 10.1016/j.msea.2020.139513

33. Ahsan MR, Tanvir ANM, Seo GJ, *et al*. Heat-treatment effects on a bimetallic additively-manufactured structure (BAMS) of the low-carbon steel and austenitic-stainless steel. *Addit Manuf*. 2020;32:101036.

doi: 10.1016/j.addma.2020.101036

34. Li K, Zhan J, Yang T, *et al*. Homogenization timing effect on microstructure and precipitation strengthening of 17-4PH stainless steel fabricated by laser powder bed fusion. *Addit Manuf*. 2022;52:102672.

doi: 10.1016/j.addma.2022.102672

35. Parizia S, Marchese G, Rashidi M, *et al*. Effect of heat treatment on microstructure and oxidation properties of Inconel 625 processed by LPBF. *J Alloys Compd*. 2020;846:156418.

doi: 10.1016/j.jallcom.2020.156418

36. Zhang Q, Liang S, Zou J, Yang Q. Interfacial microstructure of CuCr/1Cr18Ni9Ti bi-metal materials and its effect on bonding strength. *Sci China Technol Sci*. 2015;58(5):825-831.

doi: 10.1007/s11431-015-5791-6

37. Lashgari H, Adabifiroozjaei E, Kong C, Molina-Luna L, Li S. Heat treatment response of additively manufactured 17-4PH stainless steel. *Mater Charact*. 2023;197:112661.

doi: 10.1016/j.matchar.2023.112661

38. Gonzalez J, Mireles J, Stafford S, Perez M, Terrazas C, Wicker R. Characterization of Inconel 625 fabricated using powder-bed-based additive manufacturing technologies. *J Mater Process Technol*. 2019;264:200-210.

doi: 10.1016/j.jmatprotec.2018.08.031

39. Jiang D, Ning F. Bi-metal structures fabricated by extrusion-based sintering-assisted additive manufacturing. *J Manuf Process*. 2023;98:216-222.

doi: 10.1016/j.jmapro.2023.05.025

40. Kumar N, Pandey C, Kumar P. Dissimilar welding of inconel

alloys with austenitic stainless-steel: A review. *J Press Vessel Technol*. 2023;145(1):011506.

doi: 10.1115/1.4055329

41. Bina MH, Dehghani F, Salimi M. Effect of heat treatment on bonding interface in explosive welded copper/stainless steel. *Mater Des*. 2013;45:504-509.

    doi: 10.1016/j.matdes.2012.09.037

42. Liu X, Fan J, Zhang P, *et al*. Influence of heat treatment on Inconel 625 superalloy sheet: Carbides, γ", *δ* phase precipitation and tensile deformation behavior. *J Alloys Compd*. 2023;930:167522.

    doi: 10.1016/j.jallcom.2022.167522

43. Jiang W, Li G, Wu Y, Liu X, Fan Z. Effect of heat treatment on bonding strength of aluminum/steel bimetal produced by a compound casting. *J Mater Process Technol*. 2018;258:239-250.

    doi: 10.1016/j.jmatprotec.2018.04.006

44. Marchese G, Lorusso M, Parizia S, *et al*. Influence of heat treatments on microstructure evolution and mechanical properties of Inconel 625 processed by laser powder bed fusion. *Mater Sci Eng A*. 2018;729:64-75.

    doi: 10.1016/j.msea.2018.05.044

45. Floreen S, Fuchs GE, Yang WJ. The metallurgy of alloy 625. *Superalloys*. 1994;718(625):13-37.

46. Hu Y, Lin X, Li Y, *et al*. Influence of heat treatments on the microstructure and mechanical properties of Inconel 625 fabricated by directed energy deposition. *Mater Sci Eng A*. 2021;817:141309.

    doi: 10.1016/j.msea.2021.141309

47. Sabooni S, Chabok A, Feng SC, *et al*. Laser powder bed fusion of 17–4 PH stainless steel: A comparative study on the effect of heat treatment on the microstructure evolution and mechanical properties. *Addit Manuf*. 2021;46:102176.

    doi: 10.1016/j.addma.2021.102176

48. Wen Y, Gao J, Narayan RL, *et al*. Microstructure-property correlations in as-built and heat-treated compositionally graded stainless steel 316L-Inconel 718 alloy fabricated by laser powder bed fusion. *Mater Sci Eng A*. 2023;862:144515.

    doi: 10.1016/j.msea.2022.144515

49. Carrozza A, Lorenzi S, Carugo F, *et al*. A comparative analysis between material extrusion and other additive manufacturing techniques: Defects, microstructure and corrosion behavior in nickel alloy 625. *Mater Des*. 2023;225:111545.

    doi: 10.1016/j.matdes.2022.111545

50. Li C, White R, Fang XY, Weaver M, Guo YB. Microstructure evolution characteristics of Inconel 625 alloy from selective laser melting to heat treatment. *Mater Sci Eng A*. 2017;705:20-31.

    doi: 10.1016/j.msea.2017.08.058

51. An S, Eo DR, Sohn I, Choi K. Homogenization on solution treatment and its effects on the precipitation-hardening of selective laser melted 17-4PH stainless steel. *J Mater Sci Technol*. 2023;166:47-57.

    doi: 10.1016/j.jmst.2023.04.055

52. Vinod A, Warghane S, Murugan A, Balashanmugam N, Venkaiah N. Microstructure and interfacial characteristics of inconel 625-Ti6Al4V bimetallic structures produced by directed energy deposition. *J Mater Eng Perform*. 2023;33:1-12.

    doi: 10.1007/s11665-023-08250-4